Corrosion Science 228 (2024) 111744

Contents lists available at ScienceDirect

Corrosion Science

journal homepage: www.elsevier.com/locate/corsci

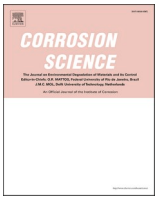

Electrochemical investigation on localised corrosion under silica sand deposit layers of carbon steel within a bespoke test cell

Raeesa Bhamji [a,*], Joshua Owen [a], Michael Huggan [a], Sabrina Marcelin [b], Bernard Normand [b], Richard Barker [a]

[a] Institute of Functional Surfaces, School of Mechanical Engineering, University of Leeds, Leeds LS2 9JT, United Kingdom
[b] Univ. Lyon, INSA-Lyon, MATEIS UMR CNRS, Bât Blaise Pascal, 7 Avenue Jean Capelle, F-69621 Villeurbanne Cedex, France

ARTICLE INFO

Keywords:
Carbon Steel
Electrochemical impedance spectroscopy
Electrochemistry
Under deposit corrosion
CO_2 corrosion
Localised corrosion

ABSTRACT

The corrosion behaviour of deep pit-like features on carbon steel under silica sand deposits has been evaluated using a bespoke localised corrosion cell. Local pH and electrochemical measurements were performed, including impedance spectroscopy and galvanic coupling. The corrosion rate of X65 carbon steel at four different recession depths up to 9 mm was evaluated in the presence and absence of a ~8 mm-thick silica dioxide deposit layer, in a carbon dioxide-saturated environment. The deposit reduced corrosion rates to approximately 1 mm·yr^{-1} and iron carbonate formed on the steel surface under the deposit due to an increase in local pH.

1. Introduction

General corrosion of carbon steel is a major obstacle in many industries, being prevalent across the energy sector. Dissolved carbon dioxide (CO_2) is present in many of these systems, creating a corrosive environment leading to the dissolution of metal ions. Carbon steel infrastructure (e.g., pipelines) utilised in energy systems can suffer from localised corrosion in CO_2-saturated environments, where preferential corrosion occurs at an increased rate in localised regions of the steel surface. When undetected and untreated, localised corrosion can produce pit-like features with penetration depths in the order of millimetres. In low velocity fluid flow systems, impurities in the form of inert sand settle on areas of the pipeline; initiating under-deposit corrosion, a process whereby settled deposits or corrosion product layers initiate enhanced corrosion under or around the deposit [1–3]. These deposits can also settle in pit-like features, thus creating a combination of under-deposit corrosion and localised corrosion, one of the main driving forces for premature pipeline failure. Settled deposits cause a range of corrosion issues, including changing the local corrosive environment under the deposits, creating a diffusion barrier for electrochemically active species and chemical inhibitors, and galvanic corrosion with exposed areas (i.e. regions not covered by the deposit) of steel [4–7].

Due to its low cost and high mechanical properties, carbon steel is still the most common material used in the energy and construction sector. Its susceptibility to corrosion in CO_2 environments is well documented and mitigation using chemical inhibitors is commonplace [8,9]. Extensive research has been conducted on the corrosion of active metals, such as carbon steel, under inert deposit layers [5,10–13]. The presence of deposit layers depresses the corrosion of the metal beneath by creating a diffusion barrier [5,10,14], however, the presence of a porous layer can be linked to localised corrosion predominantly through galvanic coupling [2]. In fully covered conditions, slight inhomogeneities in the deposit layer produce local anodes and cathodes. In other instances, deposits settle within the pipeline causing the formation of local anodes under the deposit, which is prevalent in conditions when chemical corrosion inhibitors are introduced as they are considerably more effective in inhibiting the corrosion of the exposed areas of the pipeline, compared to the covered areas of the pipeline [14,15]. Whilst previous researchers have studied the effect of under-deposit corrosion and localised corrosion individually, limited research exists on the combined effect, which forms the concept of the work in this paper.

The pioneering technique to evaluate the effects of pitting corrosion was the “pencil-pit”, the initial concept of which was introduced by Galvele [16]. The test method was further developed by Newman [17] and Turnbull *et al.* [8]. It comprised a two-component cell connected with an agar salt bridge which restricted solution mixing. A rotating carbon steel electrode was isolated from the carbon steel anode which was a pre-corroded artificial pit electrode assembly. Amri *et al.* [18]

* Corresponding author.
E-mail address: ll13r7b@leeds.ac.uk (R. Bhamji).

https://doi.org/10.1016/j.corsci.2023.111744
Received 6 September 2023; Received in revised form 29 November 2023; Accepted 2 December 2023
Available online 5 December 2023

modified this design to create an artificial pit comprising two concentric mutually insulated rods and used this technique to assess the role of acetic acid in localised corrosion via linear polarisation resistance (LPR) measurements. These methods showed benefits for the assessment of localised corrosion. However, the effect of under deposit corrosion in these environments was not explored.

In general, the introduction of settled inert deposit matter reduces intrinsic corrosion rates [6,10,11,19]. However, a shift in the local chemical environment under the deposit initiates galvanic corrosion, a phenomenon that has been studied using a zero resistance ammeter (ZRA) [1,10,20]. The direction of the galvanic current flow (i.e., to/from regions under a deposit) is dependent on the open circuit corrosion potential of the two metals. Barker *et al.* [10] evaluated the galvanic corrosion behaviour of a carbon steel specimen under a 10 mm thick layer of silica sand, coupled with a bare carbon steel specimen both corroding in the same solution of 100 g L^{-1} sodium chloride (NaCl) electrolyte at 50 °C in CO_2 saturated conditions. In the absence of corrosion inhibitors, the specimen under the deposit acted as the net cathode. The introduction of chemical corrosion inhibitors significantly increased the corrosion potential of the exposed specimen, to more anodic values, resulting in a reversal in polarity forcing the anodic dissolution of the under deposit specimen. The same effect was identified at an elevated temperature of 90 °C by Nyborg et al. [6]. This effect was related to the inability of the inhibitor to diffuse through the sand layer. The inhibitor has a much greater effect on the exposed specimen, increasing its potential, which generated a large potential difference between the under deposit and exposed specimens, driving galvanic corrosion [6,10]. Furthermore, the local pH at the metal/electrolyte interface influences the corrosion behaviour of the steel, and interfers with the formation of crystalline corrosion products on the steel surface. Han *et al.* [21] designed a mesh capped pH probe to measure the local surface pH of covered and bare carbon steel corroding in CO_2 saturated, 10 g L^{-1} NaCl electrolyte. At 25 °C the bulk electrolyte pH was 4. The pH at the bare electrode/electrolyte was 5.7, which increased to 6.3 when a 5 mm thick inert sand layer was introduced. The evolution of local physio-chemical conditions can lead to change in surface conditions and can favour the formation of iron carbonate ($FeCO_3$) but can also impact the efficiency of organic chemical inhibitors [22].

To understand the corrosion behaviour and the evolution of chemical changes within a pit like feature it is important to recap the key chemical reactions involved in the corrosion mechanism of carbon steel in CO_2 environments. It is expected that a deposit suppresses both the anodic and cathodic reactions at the steel surface, but galvanic couples can promote anodic dissolution of the under deposit specimen, particularly prevalent when chemical corrosion inhibitors are used, which act on both the anode and cathode [6,12,23]. One of the fundamental reactions in CO_2 corrosion is the dissociation of carbonic acid, via Reaction (1), creating a source of hydrogen (H^+), hydrogen carbonate (HCO_3^-) and carbonate (CO_3^{2-}) ions. Diffusion of evolved electrochemically active species (such as H^+) to the steel surface facilitates further cathodic reactions; however, a deposit layer introduces a significant diffusion barrier, resulting in the local build-up or depletion of corrosion species under the deposit. If supersaturation of Fe^{2+} is achieved, $FeCO_3$ crystallisation on the carbon steel surface can occur, represented by reaction (2)[6,7].

$FeCO_3$ is well known to reduce corrosion rates of carbon steel when it forms widely across a surface, but can also be detrimental as the entrapment of electrolyte can initiate localised corrosion, in a similar fashion to inert deposits [3,24,25]. Another criterion for $FeCO_3$ formation in general corrosion scenarios is slightly acidic or near neutral pH [26].

$$H_2CO_3 \rightleftharpoons H^+ + HCO_3^- \rightleftharpoons H^+ + CO_3^{2-} \quad (1)$$

$$Fe^{2+} + CO_3^{2-} \rightarrow FeCO_3 \quad (2)$$

The work presented in this paper examines the influence of inert silica sand on the corrosion rate of localised corrosion of carbon steel. A bespoke test cell has been designed to enable the study of carbon steel specimens at recession depths of 0 mm, 3 mm, 6 mm, and 9 mm. The themes of the localised cell designs such as the "pencil pit" have been incorporated in this study and modified to investigate localised corrosion behaviour under deposits [8,16–18]. Electrochemical techniques such as LPR, electrochemical impedance spectroscopy (EIS) and, potentiodynamic polarisation have been conducted to evaluate the corrosion behaviour of X65 carbon steel under these conditions.

2. Experimental procedure

2.1. Cell design

A bespoke test method was developed to assess the corrosion rates and mechanisms of X65 carbon steel specimens at different recession depths exposed to electrolyte and under a deposit layer. The test setup enables versatile testing conditions, such as varying temperatures, assessing multiple isolated specimens concurrently, conducting galvanic tests between exposed and under deposit specimens, or between two under deposit specimens, exploring diverse electrolyte compositions, investigating deposit properties like type, density, and mixed deposits with oils, and evaluating changes in electrolyte properties within a recess.

The cell is shown in Fig. 1, featuring a chemical resistant acetyl specimen stage (1), suspended from the cell lid (2), with the capacity to hold up to four isolated metal specimens (3) in an upright position at various depths. A polycarbonate tube of 90 mm diameter (4) was inserted into a groove on the top face of the specimen stage to contain the deposit, sealed by a nitrile O-ring. An insert was fitted into the lid for inhibitor addition directly into the centre of the cell.

To facilitate electrochemical measurements, 3 mm diameter, insulated copper wire was soldered to the reverse face of a 6 mm diameter, 6 mm thick X65 carbon steel coupon. The specimens were sealed into position in the threaded specimen holder (5) with a nonconductive two-part epoxy resin, leaving an exposed surface area of 0.28 cm^2. The threaded nylon specimen holder enables adjustment of the height of the specimens within the stage. The specimens were set to exact recessions of 0 mm (no recession), 3 mm, 6 mm and 9 mm with digital Vernier callipers. A visual demonstration of changes in specimen recession has been provided in Fig. 1(d), the depth of recession was measured from the top face of the specimen stage.

2.2. Materials and solution preparation

X65 carbon steel specimens were used as the working electrode as part of a standard 3-electrode electrochemical cell. The X65 carbon steel used in this study had a ferrite-pearlite microstructure and composition (wt%) of Fe (97.8), C (0.15), Mn (1.42), Ni (0.09), Nb (0.054), Mo (0.17), Si (0.22), V (0.06), P (0.025) and S (0.02). For electrical contact, insulated copper wire was soldered to the reverse face of the specimen before being mounted into a specimen holder and sealed with non-conducting resin. A single surface area of 0.28 cm^2 was exposed to the electrolyte. Immediately before the start of the experiment, the specimens were wet ground with silicon carbide paper progressively from P180 to P1200, degreased with acetone, rinsed with deionised water, and dried with compressed air before being mounted into the specimen stage, set to height, and placed into the test solution.

Corrosion experiments took place in 20 g L^{-1} NaCl brine solution, at 50 °C to replicate common applications where under deposit localised corrosion of carbon steel occurs. The solution of volume 1.4 L was saturated with CO_2 for a minimum of 12 h before being brought to temperature. This resulted in a starting pH of approximately 4, confirmed with an automatic temperature-compensating pH probe. All tests were carried out at atmospheric pressure. Once at temperature, the specimen stage (with or without deposit) was lowered into the pre-saturated brine solution. The solution was bubbled continuously for

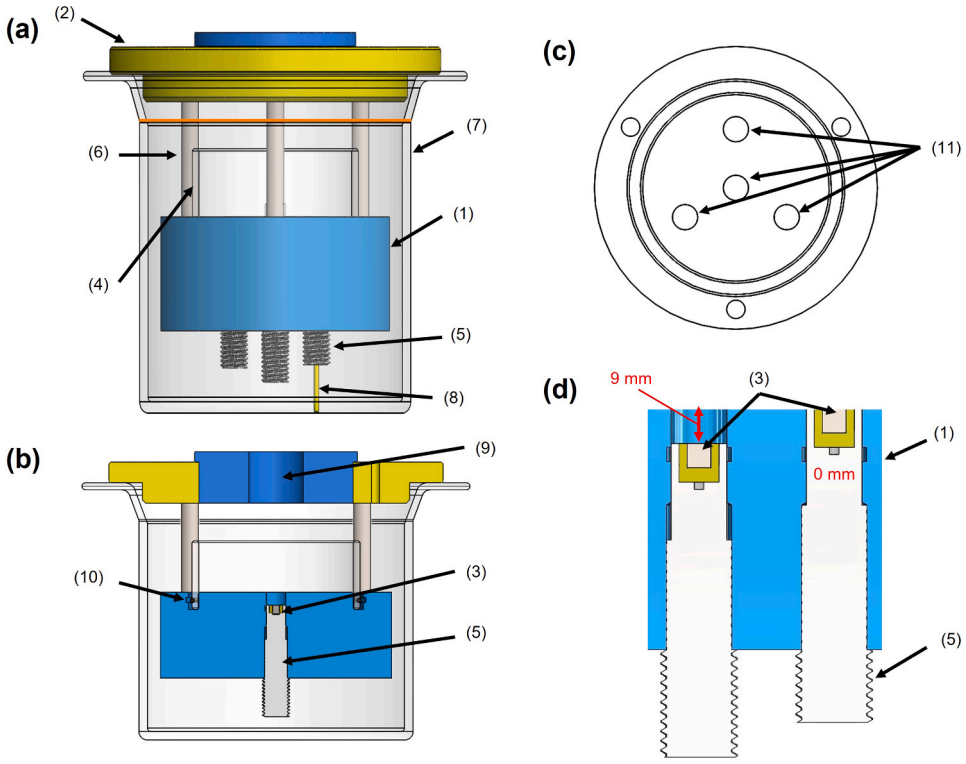

Fig. 1. Bespoke test cell for the evaluation of deep pits under thick deposit layers. (a) Complete cell highlighting key components, (b) cross section of test cell highlighting the mechanical recession of the specimen (c) top view of acetyl specimen stage showing geometry of 4 carbon steel test specimen, (d) zoomed in image of the specimen stage showing two different specimen recessions, 0 mm and 9 mm. The following labelled components include (1) acetyl specimen stage featuring 4 carbon steel specimen, (2) acrylic cell lid with a removable top insert and machined holes for a thermometer, reference electrode and wire connections, (3) X65 carbon steel specimen embedded in resin within the specimen holder, (4) polycarbonate tube to hold the deposit in position, (5) threaded nylon specimen holder, (6) threaded nylon bars to suspend the specimen stage from the cell lid, (7) 2 L glass vessel, (8) copper wire soldered to the rear of specimen for electrochemical connection to the potentiostat, (9) insert to enable chemical inhibitor addition, (10) O-ring groove and (11) specimen positions within specimen stage.

the duration of the test to ensure CO_2 saturation.

2.3. pH Measurements

In-situ pH measurements within localised regions were recorded using a Mettler Toledo™ pH electrode. It featured a glass sensing shaft measuring 3 mm in diameter. Calibration before each test was performed using Orion™ pH buffers in pH 1.68, 4.01 and 7.00. Readings were recorded every 2 s for 20 h using an OMEGA™ OMCP=PHTEMP2000 data logger with associated software.

2.4. Electrochemical measurements

A standard three electrode cell was used for electrochemical measurements comprising an X65 carbon steel working electrode (described above) and a combined electrode consisting of a silver/silver chloride (Ag/AgCl) reference electrode and a platinum counter electrode. All tests were carried out a minimum of three times to ensure reproducibility. Electrochemical measurements were conducted using an ACM Gill 4 potentiostat. The corrosion potential of the carbon steel immersed in electrolyte was measured for 20 h with LPR measurements, taken every 30 min for the duration of the 20 h test, to obtain a value of polarisation resistance (R_p, Ω cm^2). The working electrode was polarised from −15 to +15 mV vs open circuit potential (OCP), at a scan rate of 0.25 mV s^{-1}. OCP was monitored between all measurements. Charge transfer resistance (R_{ct}, Ω cm^2) was determined by deducting the electrolyte resistance (R_e, Ω cm^2) from R_p using Eq. (3).

Potentiodynamic polarisation curves were plotted after 20 h of immersion at corrosion potential. The cathodic and anodic branches were obtained consecutively, firstly in the cathodic direction from + 5 mV vs. OCP to −250 mV vs. OCP, then in the anodic direction from −5 mV to + 250 mV relative to OCP, at a sweep rate of 0.5 mVs^{-1}. The potential was corrected for ohmic drop using Ohms law. A polarisation curve of applied potential vs. current density allowed for the estimation of the anodic and cathodic Tafel constants, β_a and β_c (V), respectively, leading to the calculation of the Stern-Geary coefficient B (V), in Eq. (4). Eqs. (5) and (6) and subsequently applied to calculate the corrosion rate.

$$R_{ct} = R_p - R_e \tag{3}$$

$$B = \frac{|\beta_a||\beta_c|}{2.303(|\beta_a| + |\beta_c|)} \tag{4}$$

$$i_{corr} = \frac{B}{R_{ct}} \tag{5}$$

$$Corrosion \quad rate = \frac{Ki_{corr}M_{Fe}}{n \quad F \quad \rho} \tag{6}$$

Where K is the combination of conversion factors that convert the corrosion rate into mm yr^{-1}, equal to 3.16×10^5, M_{Fe} is the molar mass of iron (55.8 g mol^{-1}), F is the Faraday constant (96,485 C mol^{-1}), ρ is the density of X65 carbon steel (7.87 g cm^{-3}), i_{corr} is the corrosion current density (mA cm^2) and n is the number of electrons involved in the reaction as governed by the half equations of the electrochemical reactions, which in the case of Fe, $n = 2$.

For further understanding of the corrosion behaviour, electrochemical impedance measurements were recorded every four hours. A sinusoidal potential of ± 10 mV vs. OCP was applied in a frequency

range of 20^3 Hz to 10^{-1} Hz, with 10 measurements per frequency decade. The corresponding data were analysed with an equivalent circuit fitting using the Measurement Model software [27]. A value of R_e was determined from EIS measurements, discussed later, which was used to correct for IR drop in calculations of corrosion rate.

The final electrochemical technique used in this study was the assessment of galvanic corrosion using a ZRA. A larger X65 carbon steel specimen, with a surface area of 4.9 cm^2 directly exposed to the electrolyte, was coupled to a specimen beneath the deposit (area ratio of 1:18). Galvanic current and mixed potential were monitored for 20 h.

2.5. Surface analysis

To visually assess the extent of corrosion and any corrosion product formation, SEM images were collected using a Hitachi TM3030 Benchtop SEM. Micrographs were acquired using an accelerated voltage of 15 kV in secondary electron mode. For sand particles, the grain size of individual particles was measured as highlighted below. X-Ray diffraction (XRD) patterns for the assessment of $FeCO_3$ were made using a Siemens Bruker D8 Advanced multipurpose diffractometer by employing 40 kV ($K\alpha_{1+2}$) Cu radiation over a scattering angle range of $20° < 2\theta < 70°$. A targeted scan between $31° < 2\theta < 33°$ was also taken which was sufficient for the magnification of a dominant $FeCO_3$ peak which appears at approximately 32° [3], according to the International Centre for Diffraction Data (ICDD) reference 04–015.

2.6. Deposit properties and preparation

Extra pure SiO_2 sand (20–30 mesh, Fisher Scientific) was used in all under deposit testing conditions. To ensure the purity of the sand and consistency between batches, the required quantity of sand was immersed in 1 M sodium hydroxide solution, sonicated for 15 min, and neutralised with 5 M hydrochloric acid. The particles were then rinsed with deionised water and allowed to dry overnight at 37 °C in an oven. A total of 100 g of sand was added to the stage before lowering into the saturated electrolyte solution. This resulted in a deposit layer thickness of 8 mm for specimens positioned at a 0 mm pit depth, which increased incrementally with specimen recession. The average sand particle size was 800 μm, determined using a Malvern Mastersizer 300 laser diffraction particle sizer, and confirmed using a Hitachi TM3030Plus Autostage SEM. The mastersizer distribution and sand particle images are given in Fig. 2.

3. Results and discussion

3.1. Under deposit corrosion rates and electrochemical behaviour

The corrosion rate of the X65 carbon steel specimen determined from LPR measurements, both in the absence and presence of an inert deposit was evaluated at 50 °C in 20 g L^{-1} NaCl electrolyte solution saturated with CO_2 with the starting pH ~4. Fig. 3 reports the R_{ct}^{-1} and average corrosion rate at different recession depths, with error bars representing the standard deviation from a minimum of three repeat experiments. To compensate for ohmic drop the potential data was corrected using R_e values of 6.0 Ω·cm^2 (0 mm), 7.0 Ω·cm^2 (3 mm), 8.0 Ω·cm^2 (6 mm) and 9.5 Ω·cm^2 (9 mm) obtained from impedance measurements (shown and discussed later). The potentiodynamic polarisation curves at all specimen recession depths were similar, as seen in Fig. 4, giving B values of 22.7 ± 1.7 mV, determined by Tafel extrapolation. The values of R_p obtained from LPR measurements were similarly corrected for R_e, giving R_{ct} which was used to calculate corrosion rate via Eqs. (5) and (6). The corrosion rate profile obtained from LPR measurements in the absence of a deposit in Fig. 3(a) showed a steady increase from approximately 3 mm yr^{-1} to 4.5 mm yr^{-1} over 20 h, which is synonymous with the revealing of a porous iron carbide (Fe_3C) network [28]. The conductive Fe_3C network enhances corrosion rates by establishing micro galvanic cells with the ferrite phases in the steel microstructure [24,29].

The impact of an inert deposit layer in direct contact with the specimen was assessed by covering the specimen in 100 g of pure, inert SiO_2. The sand was not compressed or compacted in any way. This gave a corresponding deposit thickness which naturally varied with specimen recession, starting with a thickness of 8 mm at 0 mm specimen recession. Tafel behaviour, given in Fig. 4, again showed very similar behaviour at different specimen recessions resulting in a B value of 24.9 mV at all depths. No significant difference in OCP was observed between covered and uncovered specimens, suggesting the deposit had no significant impact on the nature of the reactions taking place. The deposit is likely causing a surface blocking effect, creating a diffusion barrier for corrosive ions [7]. The sand deposit acts as a barrier preventing or delaying the accessibility of corrosive ions to the steel surface, this manifests as a limitation to both the anodic and cathodic reactions, resulting in a lower corrosion rate of approximately 1 mm yr^{-1}, as seen in Fig. 3(b).

It is clear from Fig. 5(a) that the OCP of carbon steel in the absence of a deposit exhibits a very small increase over time at all depths, attributed

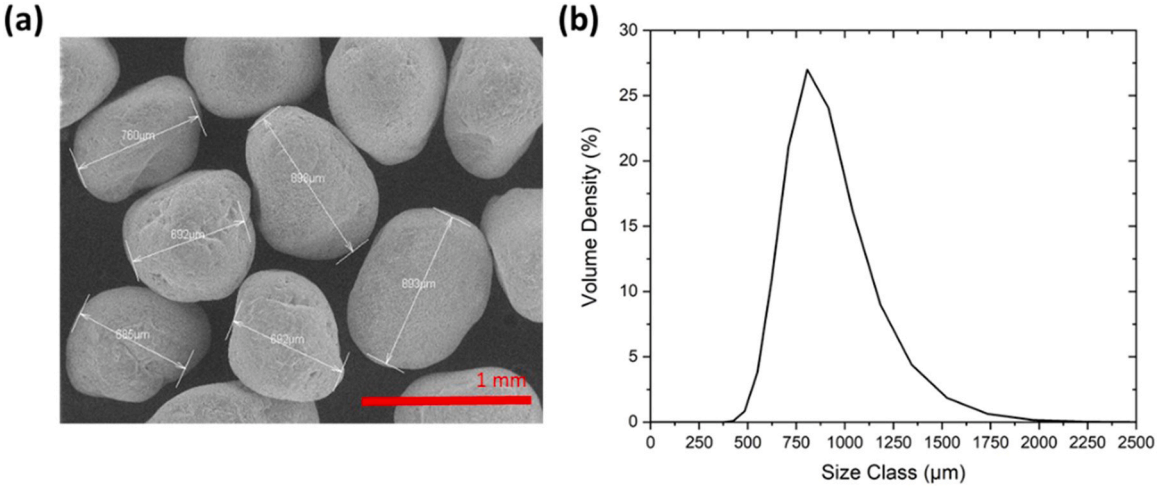

Fig. 2. a) SEM image of sand particles and b) laser diffraction size distribution taken on a Melvern Mastersizer 300 showing the average particle size distribution.

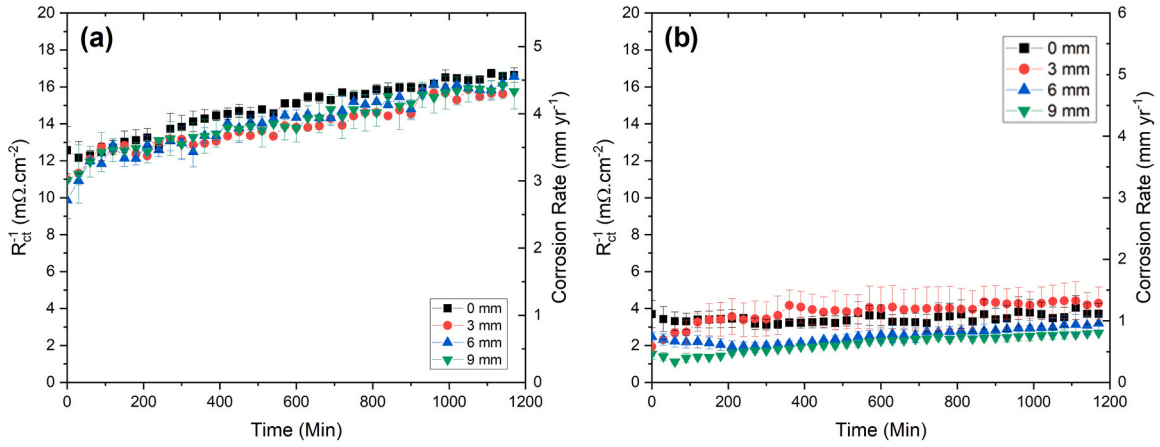

Fig. 3. R_{ct}^{-1} and corresponding corrosion rates, determined from LPR measurements of carbon steel specimens at depths of 0 mm (black line), 3 mm (red line), 6 mm (blue line), and 9 mm (green line) (a) without a sand deposit layer and (b) with a sand deposit layer, at 50 °C and pH 4 in a CO_2 saturated, 20 g L^{-1} NaCl electrolyte. Compensation has been made for ohmic drop. Corrosion rates were calculated using B values of 22.7 mV and 24.9 mV for (a) and (b) respectively.

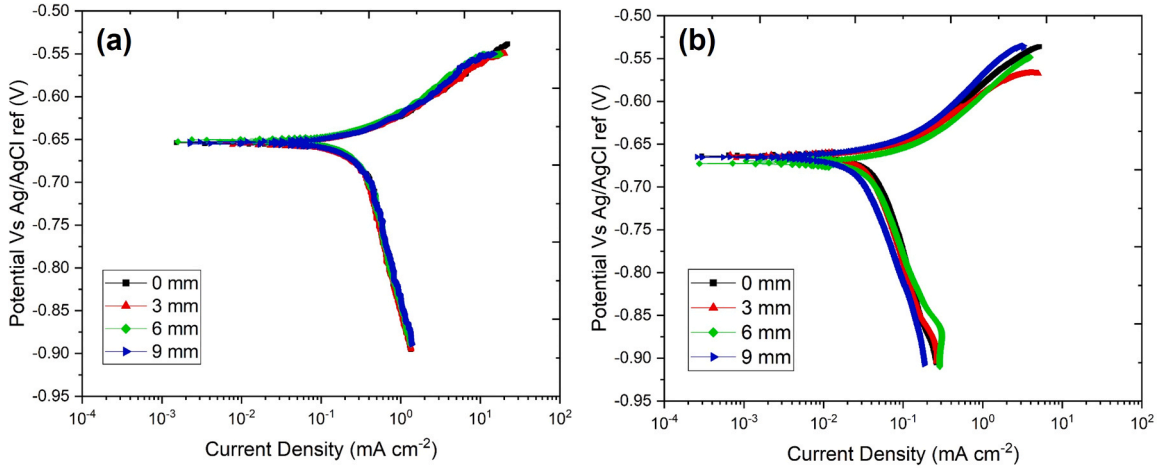

Fig. 4. Potentiodynamic polarisation curves for carbon steel specimens at depths of 0 mm (black line), 3 mm (red line), 6 mm (blue line), and 9 mm (green line) a) without a sand deposit layer and b) with a sand deposit layer, against an Ag/AgCl reference electrode at 50 °C and pH 4 in a CO_2 saturated, 20 g L^{-1} NaCl electrolyte. Compensation has been made for ohmic drop.

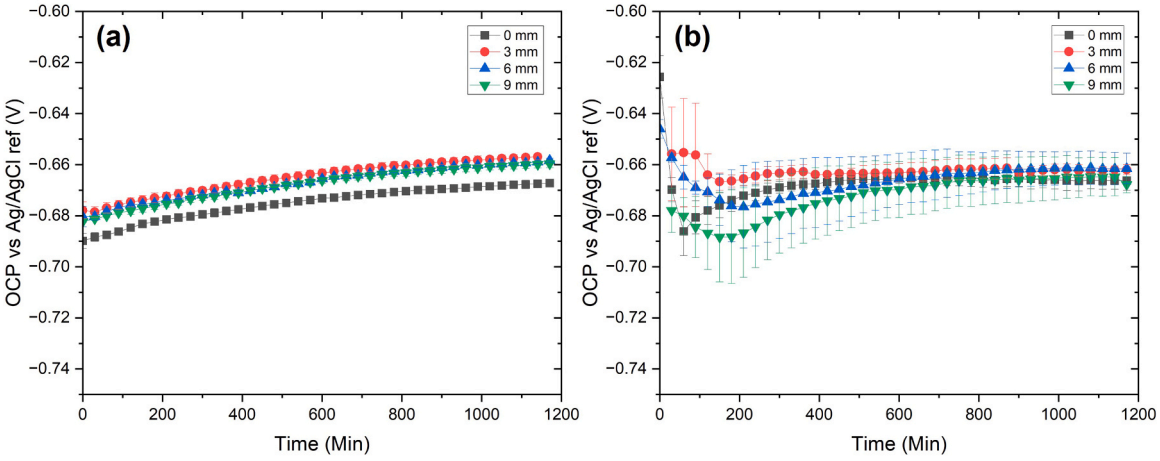

Fig. 5. Open circuit potential Vs Ag/AgCl reference of carbon steel specimens at recession depths of 0 mm (black line), 3 mm (red line), 6 mm (blue line), and 9 mm (green line) of a) without a sand deposit layer and b) with a sand deposit layer, at 50 °C and pH 4 in a CO_2 saturated, 20 g L^{-1} NaCl electrolyte.

to the revealing of a Fe_3C network establishing a galvanic couple with the ferrite phases [24,29–31]. In contrast, specimens which are covered with a thick deposit layer require a stabilisation period before reaching a steady corrosion rate. This highlighted possible changes in the properties of the interfacial electrolyte. The OCP then reached a minimum value before increasing to give a final OCP of approximately −0.67 V vs Ag/AgCl.

3.2. EIS evaluation of corrosion mechanisms

EIS measurements of the carbon steel electrodes at varying depths in the absence of a deposit were taken over 20 h to evaluate the corrosion behaviour at the steel/electrolyte interface [32]. The Nyquist spectra for uncovered specimens at recession depths of 0 mm, 3 mm, 6 mm and 9 mm are provided in Fig. 6, with the solid lines representing the equivalent electrical surface (discussed later). The Kramers-Kronig conditions were verified for each data set, using the method described by Boukamp *et al.* [33] with a 90 % confidence interval. Data non-compliant with Kramers-Kronig conditions of linearity and stability were omitted from analysis and not shown in subsequent data plots.

The Nyquist spectra featured one single capacitive loop representative of the impedance associated with the charge transfer corrosion process. This is typically represented in equivalent electrical circuits as R_e in series with an R_{ct}, which is in parallel with a constant phase element (CPE), denoted by Q_{dl} to represent non-ideal capacitive behaviour of the electrical double layer [34]. The Q_{dl} is the differential capacity at the interface which includes the contribution of α_{dl} which is a dimensionless parameter associated with frequency dependence of impedance. This circuit is shown in Fig. 6(a), and is referred to as the simplified Randles circuit [34]. The equivalent circuit and analysis are discussed extensively below.

The diameter of the semi-capacitive loop was similar across all recession depths, indicating similar corrosion rates. It is worth noting that the diameter of the loop decreases with time corresponding to a reduction in R_{ct} and thus an increase in corrosion rate, characteristic of the revealing of a porous iron carbide network [24,28,29]. There is also a distinct depression in the amplitude of the loop indicating a deviation from a pure capacitor to CPE behaviour, suggesting surface heterogeneity [34].

To represent the frequency distribution of the Nyquist plots and identify high frequency behaviour, Bode phase plots were corrected for solution resistance by applying Eq. (7).

$$\phi_{corrected} = \tan^{-1}\left(\frac{Z''}{Z' - R_e}\right) \tag{7}$$

CPE behaviour was observed in the high frequency region (i.e. $\phi_{corrected} < -90°$ as frequency tends to infinity) of the R_e corrected Bode phase plot, shown in Fig. 7, which have been corrected for the effects of solution resistance by applying Eq. (7)). There was no significant change in behaviour with recession depth, with no identifiable change in the reaction mechanism. At all recession depths $\alpha_{dl} \sim 0.7$, governed by the linear region between the high and low frequency asymptotes, expressing corrosion behaviour attributed to surface heterogeneity and a charge-transfer reaction [34,35]. Some dispersion of the phase angle

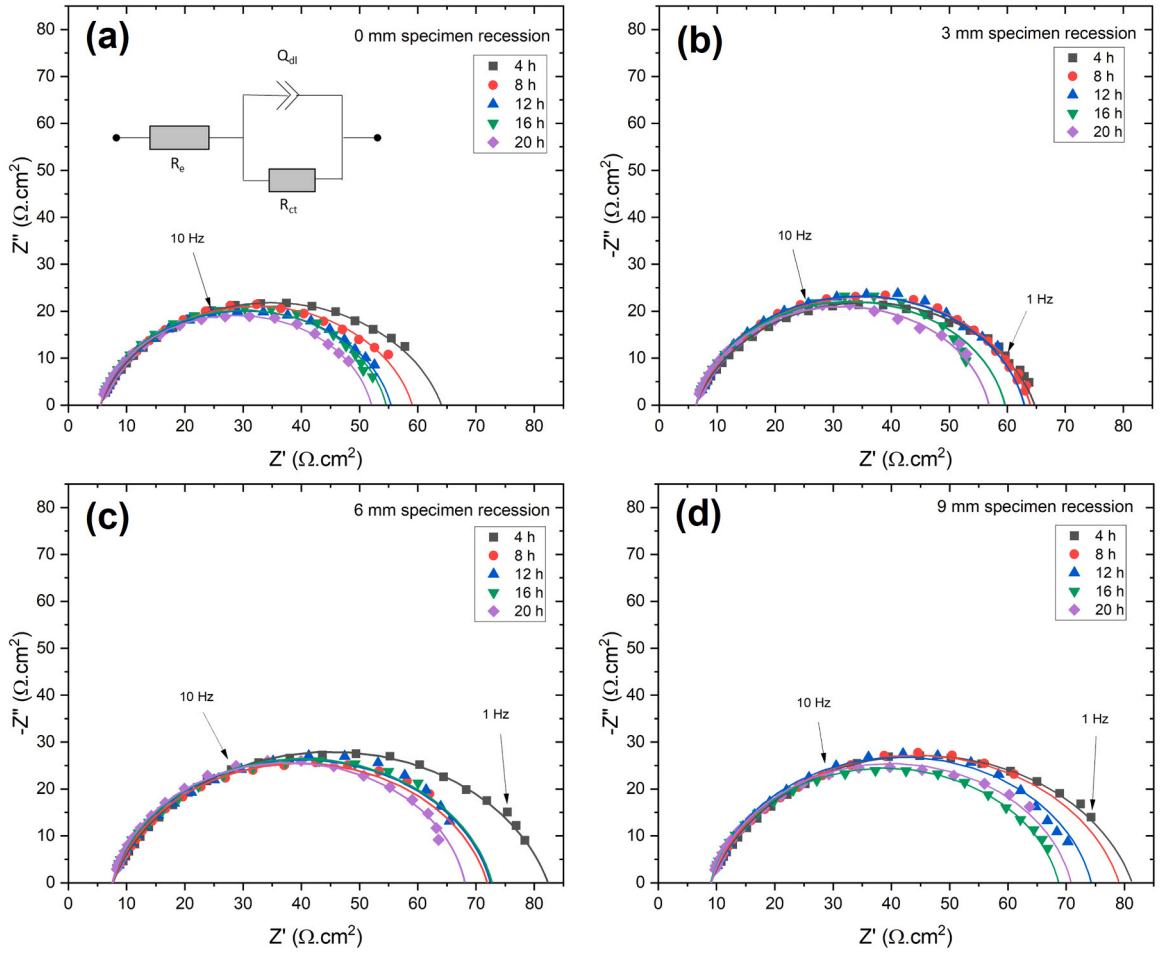

Fig. 6. Nyquist impedance diagrams over 20 h obtained at the corrosion potential for carbon steel specimens immersed in a CO_2 saturated, 20 g L^{-1} NaCl electrolyte at 50 °C and pH 4 in the absence of a deposit. Specimens were at recession depths of (a) 0 mm (no recession), (b) 3 mm, (c) 6 mm and (d) 9 m. Data was modelled using the equivalent electrical circuit in (a) and corresponding model data are represented as solid lines.

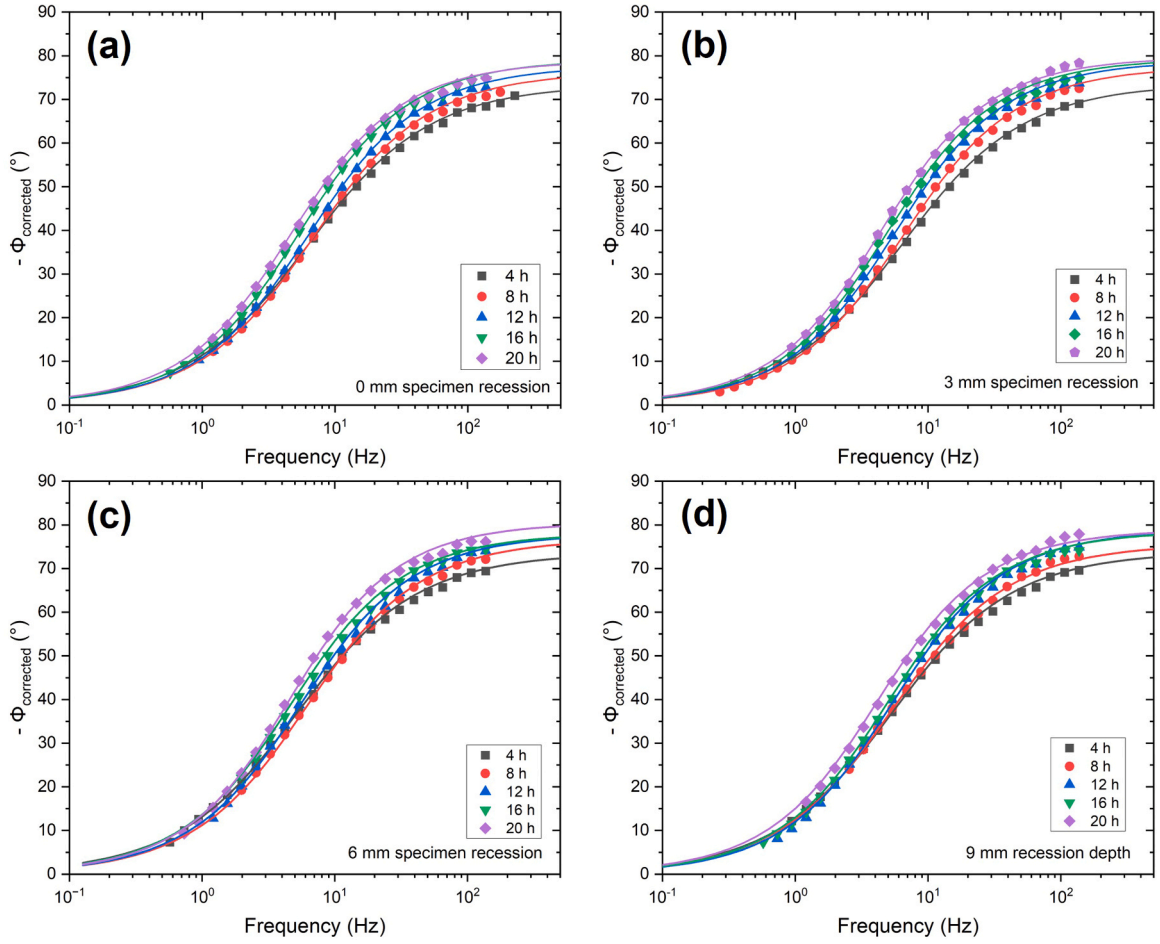

Fig. 7. Solution resistance corrected Bode phase angle diagrams as a function of frequency obtained for the carbon steel in the absence of deposit, comparing different receding depths for (a) 0 mm (no recession), (b) 3 mm, (c) 6 mm and (d) 9 mm. The measurements are carried out at corrosion potential in the EIS measurements of the carbon steel specimens were taken at 4 h intervals in a 50 °C and pH 4 in a CO_2 saturated, 20 g L^{-1} NaCl electrolyte. Obtained equivalent electrical circuit fits are represented as solid lines corresponding to the fit result from the electrical equivalent circuit presented in Fig. 6.

was observed at high frequencies, due to the sensitivity of selecting R_e and applying Eq. (6). The Bode phase plot showed excellent goodness of fit which was of the order of 10^{-5} in all cases. Uncorrected Bode magnitude and phase plots have been provided in the Supplementary Material.

To understand how the carbon steel corrosion behaviour changed under a thick deposit layer, electrochemical impedance measurements were similarly performed in the presence of 100 g SiO_2 deposit. The Nyquist plots for the covered specimens are provided in Fig. 8, where it is immediately evident the size of the loop overall was significantly larger in comparison to uncovered specimens (Fig. 6), corresponding to a larger R_{ct}. There is a shift in electrolyte resistance (R_e) which was governed by the first intersection of the x-axis (or by extrapolation where this intersection was not observed). It was attributed to the restricted diffusion of electrochemically active species through the deposit layer. Only a single capacitive loop was identified, and it is attributed to a pure CPE behaviour as shown in the corrected Bode phase plots in Fig. 9. Interestingly the diameter of the semi-capacitive loop increases with time, corresponding to a decrease in corrosion rate. This could be attributed to the formation of $FeCO_3$ and/or a significant change in local chemical properties such as pH [7,21,36]. A protective layer of non-conductive $FeCO_3$ is expected to reduce corrosion rates by blocking active sites and potentially acting as an additional diffusion barrier between the steel surface and the bulk electrolyte. De Motte *et al.* [37] demonstrated that the presence of a protective $FeCO_3$ layer alters the electrochemical characteristics of the metal, as evidenced by the impedance diagrams exhibiting two time constants, one corresponding to the behaviour of the electrical double layer in the high frequency region, whilst the other represents the behaviour and corresponding resistance provided by the $FeCO_3$ layer in the low frequency range. However, this effect was not identified in the work presented in Fig. 9 indicating the surface coverage of $FeCO_3$ is insufficient to provide significant corrosion protection, likely due to the lower pH (5–6, discussed later) and temperature (50 °C) compared to the conditions studied by De Motte *et al.* [37] (pH 6 – 6.6, temperature 80 °C).

3.3. Equivalent electrical circuit analysis

A simplified Randles circuit was used to model the data to an equivalent electrical circuit for the uncovered specimens, which corresponds graphically to the circuit shown in Fig. 6(a). This equivalent electrical circuit is widely used to represent the corrosion of carbon steel in aqueous CO_2 environments when no surface layers are present [34,37,38].

Table 1 presents the Randles equivalent electrical circuit fitting parameters for uncovered specimens. The double layer capacitance (C_{dl}) shown in Table 1 was calculated using Eq. (8) introduced by Brug *et al.* [39] and used in Eq. (9) to determine the active surface area, (S_a, %) [37,40]. S_a is the ratio between C_{dl} at the start of the test and time, t, into the test, expressed as a percentage of the original surface area. For all calculations, 4 h is taken as the baseline, being the first impedance measurement recorded. S_a has been used successfully to evaluate surface

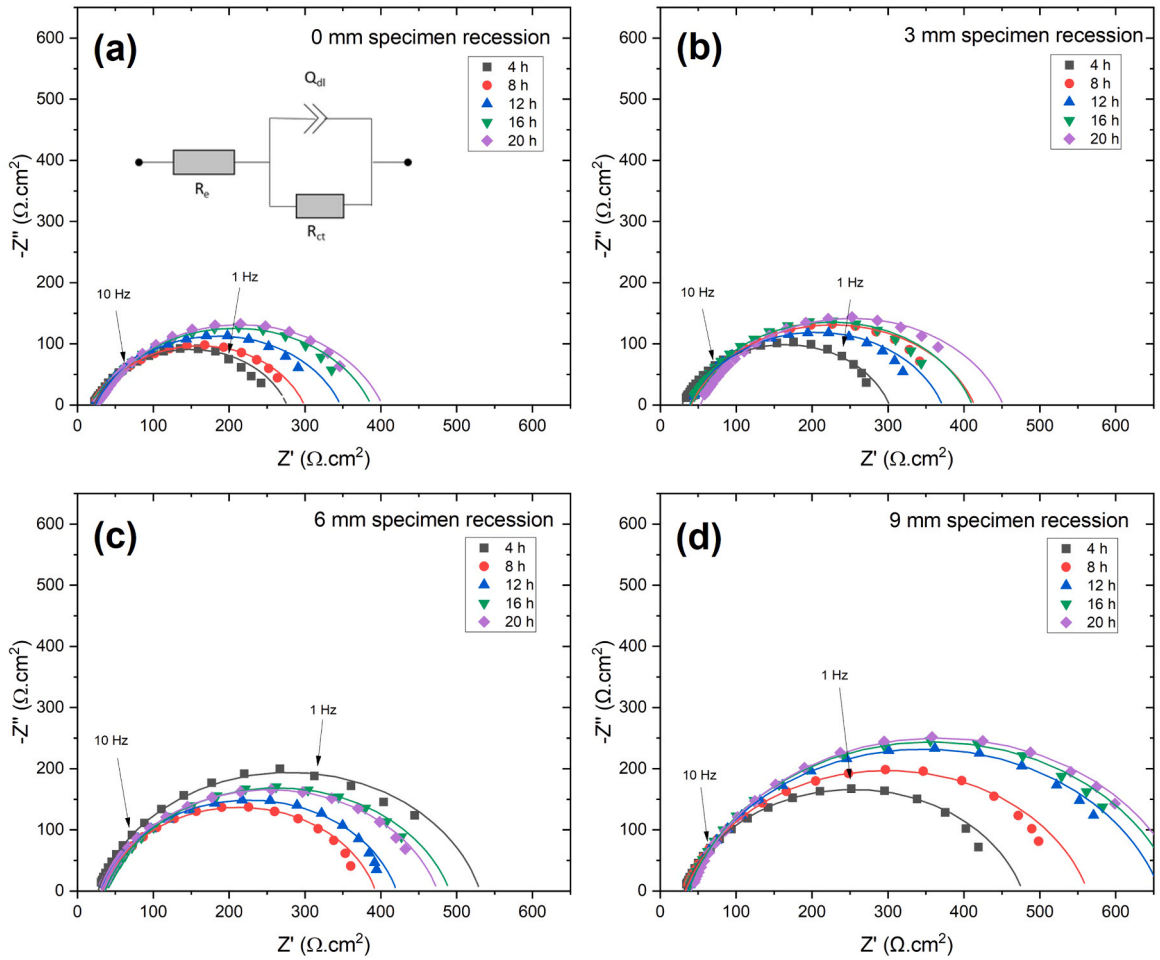

Fig. 8. Nyquist impedance diagrams obtained during time for the carbon steel over 20 h in the presence of a deposit comparing carbon steel specimens at receding depths of a) 0 mm (no recession), b) 3 mm, c) 6 mm and d) 9 mm. EIS measurements of the carbon steel specimen were taken at 4 h intervals in a 50 °C and pH 4 in a CO_2 saturated, 20 g L^{-1} NaCl electrolyte. Obtained equivalent electrical circuit fits are represented as solid lines correspond to the fit result by using the electrical equivalent circuit presented in (a).

coverage with corrosion product layers, and the blocking of anodic and cathodic reactive sites [37,41].

$$C_{dl} = \frac{1}{Q_{dl}}\left(R_e^{-1} + R_{ct}^{-1}\right)^{\frac{1-\alpha_{dl}}{\alpha_{dl}}} \tag{8}$$

$$S_a = \frac{C_{dl(t)}}{C_{dl(0)}} \times 100 \tag{9}$$

The capacitive loop in Fig. 6 for the exposed specimens decreased in size with time, corresponding to a decrease in R_{ct}, which is an indication of an increase in the corrosion rate. This is synonymous with the trend given by LPR measurements and consistent with the revealing of a porous Fe_3C network, as seen in Fig. 10 [24,30,31]. This is confirmed in the equivalent electrical circuit analysis shown in Table 1. The value of R_{ct} showed a general increase with specimen recession depth in Table 1, which is likely related to the increase in ohmic resistance due to the geometry of the test cell. The corrosion rate was calculated using the R_{ct} values obtained from EIS fitting parameters, a Stern-Geary coefficient of 23 mV and Eqs. (5) and (6), yielding very similar results to those obtained from LPR measurements, shown in Fig. 3.

In all cases $\alpha_{dl} < 1$ which shows deviation from ideal capacitive behaviour. The C_{dl} calculated using Eq. (8) increased over time with similar results and trends between all conditions. This corresponded to an increase in S_a calculated using Eq. (9), with C_{dl} at t = 0 represented by the first EIS measurement of the test (recorded at 4 h to enable stabilisation in the EIS response). S_a increased to above 100% due to the revealing of Fe_3C [28]. The inverse relationship between C_{dl} and R_{ct} is well established and indeed holds true in this case; an extension of this relationship governs that C_{dl} and S_a are directly proportional. The increase in both parameters with time was expected due to surface roughening effects and the revealing of a conductive porous Fe_3C network on the steel surface [24,29]. A constant product between R_{ct} and C_{dl} indicates the electrochemical impedance response is independent of S_a and related to the charge-transfer reactions at the steel surface. The values given in Table 1 show that the time constant (R_{ct}·C_{dl}) increases with time indicating the corrosion process is being controlled by both changes in surface area and changes in the ionic species within the double layer [37,41]. As the depth of the specimen increases, S_a decreases over time signalling that the rate of the anodic and cathodic reactions decreases with specimen recession depth. As specimen recession increases the corrosion process is impeded, with or without the deposit.

Several options exist for equivalent electrical circuits when a deposit or an inert surface layer is in contact with the surface. De Motte *et al.* [37] observed a surface blocking effect when $FeCO_3$ formed on carbon steel surfaces represented by a simple Randles circuit, with an additional capacitive loop forming in the low frequency region when high surface coverage was achieved, attributed to diffusion impedance. Hoseinieh *et al.* [42] implemented a two time constant circuit, with one time constant at low frequency representing charge transfer effects and the second time constant at high frequency representing the pores in the calcareous deposits. A single time constant was observed in Figs. 8 and 9, therefore

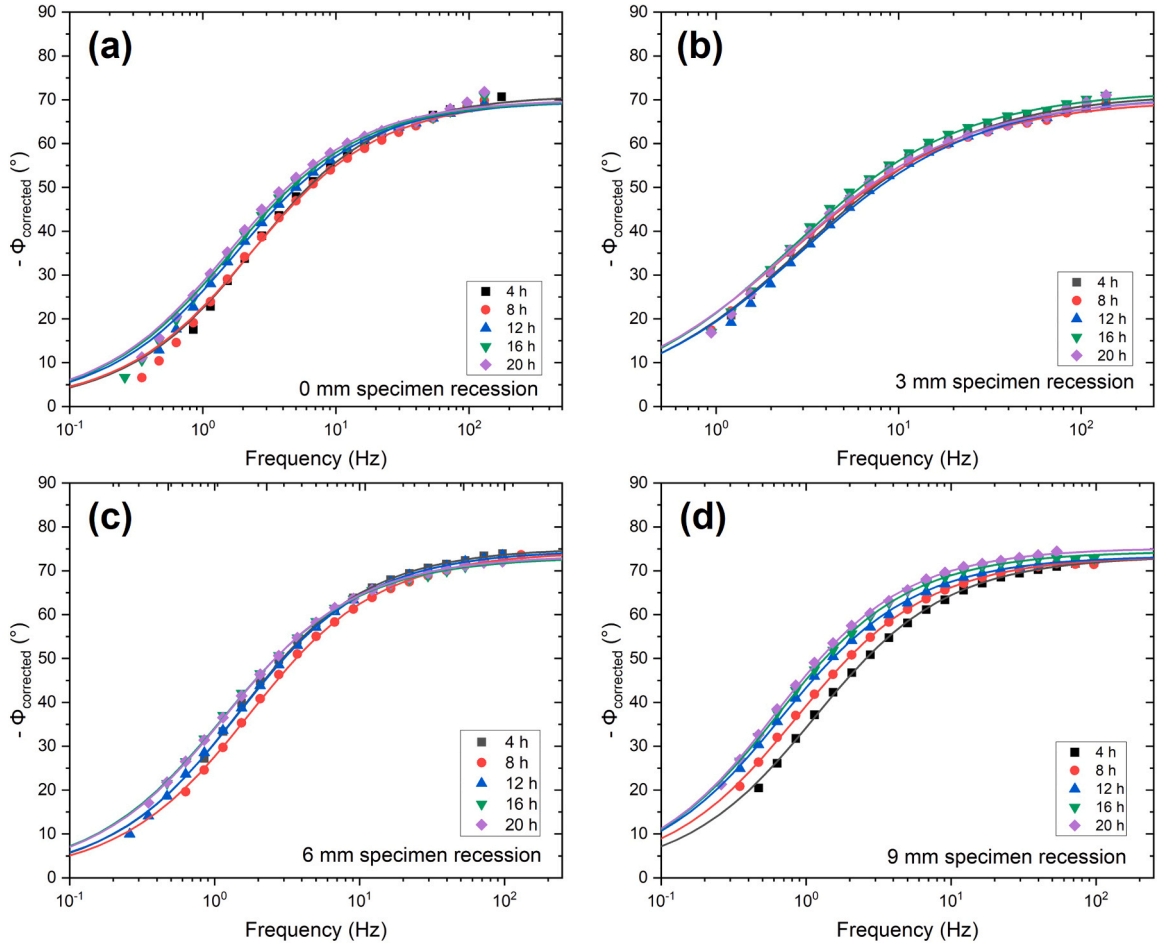

Fig. 9. Solution resistance corrected Bode phase angle diagrams as a function of frequency obtained for the carbon steel in the presence of deposit, comparing different receding depths for (a) 0 mm (no recession), (b) 3 mm, (c) 6 mm and (d) 9 mm. The measurements are carried out at corrosion potential in the EIS measurements of the carbon steel specimens were taken at 4 h intervals in a 50 °C and pH 4 in a CO_2 saturated, 20 g L^{-1} NaCl electrolyte. Obtained equivalent electrical circuit fits are represented as Solid lines corresponding to the fit result from the electrical equivalent circuit presented in Fig. 6.

there was not a significant capacitive contribution of the deposit layer. The theoretical capacitance of the layer in this study was calculated using the following equation:

$$C_{layer} = \varepsilon\varepsilon_0 A \times 10^6 \quad (10)$$

Where ε is the dimensionless dielectric constant of the deposit layer, 3.7 for SiO_2 [34], ε_0 is the permittivity in a vacuum (8.85 $\times 10^{-14}$ F.cm^{-2}) and A, the surface area of the specimen (0.28 cm^2).

The sand layer was not observed as a separate loop, negating the need for additional circuit elements. This was justified by applying Eq. (10) to calculate a theoretical capacitance of the order of 10^{-9} μF.cm^{-2} for an 8 mm thick silica sand layer. This value was several orders of magnitude lower than C_{dl} for the metal specimen in Table 1, explaining why the effect of the layer was not observed as a separate loop.

Table 2 presents the Randles electrical equivalent circuit fitting parameters for specimens covered with a deposit layer. The value of C_{dl} was calculated using Eq. (8) by Brug *et al.* [39] and showed no significant change over time or recession depth. The corresponding S_a was calculated using Eq. (9) and showed a smaller increase over time than for an uncovered specimen. The corresponding time constant, R_{ct}·C_{dl}, is governed by the changes in Rct over time which remained relatively constant throughout the test, indicating no significant change in corrosion behaviour. The corrosion rate was calculated using the R_{ct} values obtained from EIS fitting parameters and a Stern-Geary coefficient of 23 mV, yielding very similar results to the corrosion rate calculated from LPR measurements, shown in Fig. 3.

3.4. Surface analysis

Surface analysis techniques including SEM and XRD were used to assess the extent of visual corrosion on the surface. Fig. 10 shows the SEM imaging of the exposed specimens after 20 h in CO_2 saturated, 20 g L^{-1} NaCl electrolyte at 50 °C. A porous layer of Fe_3C can be identified which agrees with the increase in corrosion rate observed in electrochemical methods.

Alternatively, SEM imaging of the deposit-covered specimen after 20 h corrosion (Figs. 11) showed the formation of $FeCO_3$ within a Fe_3C network. Heterogeneous $FeCO_3$ formation occurred in small clusters, highlighting non-uniform corrosion of carbon steel under an SiO_2 deposit. The presence of $FeCO_3$ can contribute to the reduction in corrosion rate as the $FeCO_3$ crystals block active anodic and cathodic reaction sites (which may already be greatly reduced as a result of the deposit). However, the presence of poorly adhered or heterogeneous coverage of $FeCO_3$ could initiate further localised corrosion [3,31].

The presence of $FeCO_3$ was verified by XRD (Fig. 12). A scan range of 2° within the 104 crystal plane of $FeCO_3$ was chosen to emphasise the dominant peak. A clear peak can be seen at approximately 32° for 3 mm, 6 mm and 9 mm depths which corresponds to crystalline $FeCO_3$. This peak is not visible at 0 mm depth which corresponds with the SEM

Table 1
Fitting parameters of a simplified Randles circuit for uncovered specimen after 20 h of corrosion in a 50 °C, pH 4, CO_2 saturated, 20 g L^{-1} NaCl electrolyte.

Specimen recession	Parameter	4 h	8 h	12 h	16 h	20 h
0 mm	**R_e ($\Omega.cm^{-2}$)**	6.0 ± 0.4	6.0 ± 0.3	6.0 ± 0.3	6.0 ± 0.3	6.0 ± 0.4
	α_{dl}	0.82 ± 0.003	0.85 ± 0.002	0.87 ± 0.005	0.88 ± 0.002	0.89 ± 0.010
	Q_{dl} / 10^{-4} ($F.cm^{-2})^{\alpha}$	8.0 ± 0.4	7.3 ± 0.4	7.5 ± 0.7	8.3 ± 0.7	9.3 ± 0.1
	R_{ct} ($\Omega.cm^{-2}$)	65.2 ± 5.0	61.6 ± 5.8	58.7 ± 6.3	56.1 ± 5.3	53.0 ± 4.7
	C_{dl} ($\mu F.cm^{-2}$)	237 ± 11	273 ± 12	329 ± 20	394 ± 37	478 ± 39
	$R_{ct}.C_{dl}$ (ms)	15 ± 0.6	17 ± 1.0	19 ± 1.1	22 ± 0.5	25 ± 0.6
	S_A (%)	100 ± 0	115 ± 0	139 ± 20	166 ± 8	201 ± 8
	Corrosion rate (mm yr^{-1})	4.1 ± 0.3	4.3 ± 0.4	4.5 ± 0.5	4.7 ± 0.5	5.0 ± 0.5
3 mm	**R_e ($\Omega.cm^{-2}$)**	7.0 ± 0.5	7.1 ± 0.5	7.1 ± 0.6	7.0 ± 0.5	7.0 ± 0.5
	α_{dl}	0.83 ± 0.009	0.86 ± 0.003	0.88 ± 0.002	0.88 ± 0.009	0.89 ± 0.004
	Q_{dl} / 10^{-4} ($F.cm^{-2})^{\alpha}$	6.8 ± 1.2	6.3 ± 0.6	6.4 ± 1.0	7.2 ± 1.6	8.1 ± 2.0
	R_{ct} ($\Omega.cm^{-2}$)	79.9 ± 17.3	76.3 ± 15.5	73.5 ± 14.1	72.7 ± 18.3	69.9 ± 15.1
	C_{dl} ($\mu F.cm^{-2}$)	223 ± 26	255 ± 31	297 ± 49	348 ± 74	410 ± 93
	$R_{ct}.C_{dl}$ (ms)	17 ± 1.9	19 ± 1.6	21 ± 0.6	24 ± 1.4	27 ± 0.6
	S_A (%)	100 ± 0	114 ± 1	132 ± 7	154 ± 15	212 ± 50
	Corrosion rate (mm yr^{-1})	3.5 ± 0.8	3.6 ± 0.7	3.7 ± 0.7	3.8 ± 1.0	4.0 ± 0.9
6 mm	**R_e ($\Omega.cm^{-2}$)**	8.2 ± 0.4	8.2 ± 0.4	8.3 ± 0.5	8.3 ± 0.5	8.3 ± 0.5
	α_{dl}	0.81 ± 0.003	0.86 ± 0.007	0.88 ± 0.008	0.87 ± 0.004	0.90 ± 0.005
	Q_{dl} / 10^{-4} ($F.cm^{-2})^{\alpha}$	7.5 ± 0.2	6.2 ± 0.5	6.1 ± 0.7	7.0 ± 0.8	7.1 ± 0.7
	R_{ct} ($\Omega.cm^{-2}$)	77.8 ± 2.9	79.7 ± 9.4	77.3 ± 9.4	76.0 ± 7.6	70.7 ± 8.7
	C_{dl} ($\mu F.cm^{-2}$)	230 ± 10	251 ± 18	282 ± 23	327 ± 29	383 ± 42
	$R_{ct}.C_{dl}$ (ms)	18 ± 0.4	20 ± 1.6	22 ± 0.9	25 ± 0.6	27 ± 0.8
	S_A (%)	100 ± 0	109 ± 4	122 ± 6	142 ± 7	179 ± 19
	Corrosion rate (mm yr^{-1})	3.4 ± 0.1	3.4 ± 0.5	3.5 ± 0.4	3.5 ± 0.4	3.8 ± 0.5
9 mm	**R_e ($\Omega.cm^{-2}$)**	9.6 ± 0.4	9.6 ± 0.4	9.6 ± 0.4	9.6 ± 0.4	9.6 ± 0.4
	α_{dl}	0.83 ± 0.016	0.86 ± 0.008	0.87 ± 0.005	0.88 ± 0.005	0.89 ± 0.014
	Q_{dl} / 10^{-4} ($F.cm^{-2})^{\alpha}$	6.3 ± 1.1	5.9 ± 0.9	5.8 ± 0.9	6.3 ± 0.1	6.6 ± 0.2
	R_{ct} ($\Omega.cm^{-2}$)	98.3 ± 19.0	93.3 ± 20.5	88.5 ± 18.2	89.6 ± 24.1	90.8 ± 23.2
	C_{dl} ($\mu F.cm^{-2}$)	210 ± 33	241 ± 33	271 ± 46	306 ± 68	348 ± 84
	$R_{ct}.C_{dl}$ (ms)	20 ± 2	22 ± 2	23 ± 1	26 ± 2	30 ± 1
	S_A (%)	100 ± 0	116 ± 12	129 ± 12	145 ± 17	177 ± 43
	Corrosion rate (mm yr^{-1})	2.8 ± 0.6	3.0 ± 0.7	3.1 ± 0.7	3.2 ± 0.9	3.1 ± 0.8

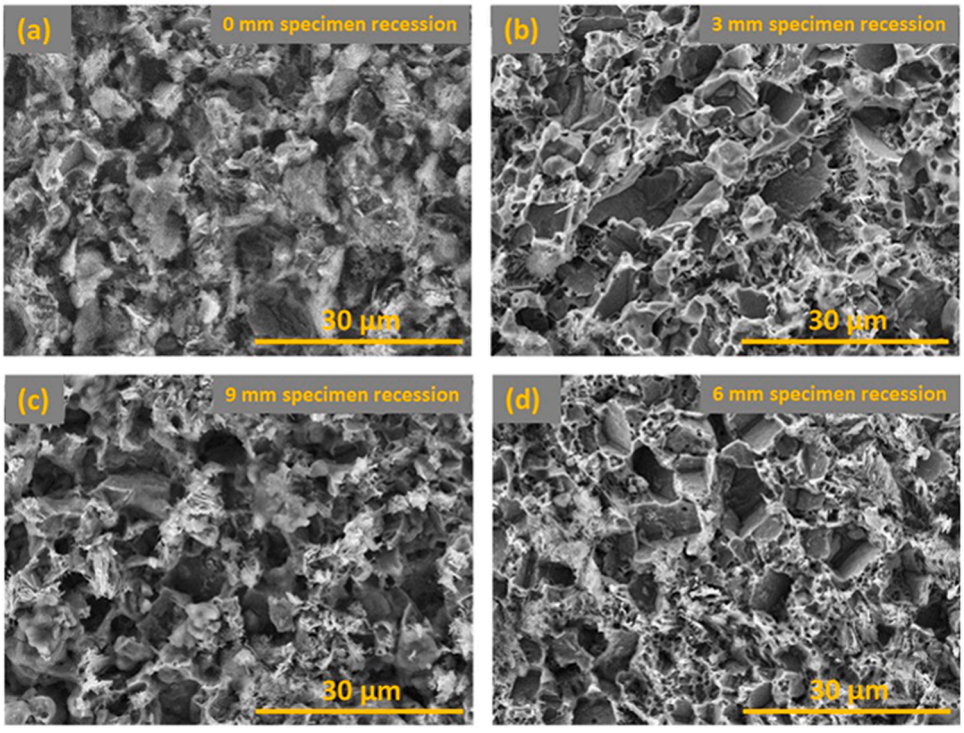

Fig. 10. SEM images taken on Hitachi TM3030Plus Autostage SEM at 2500X magnification of exposed X65 carbon steel specimen (absence of SiO_2 deposit) after 20 h of corrosion in a 50 °C, pH 4, CO_2 saturated, 20 g L^{-1} NaCl electrolyte. a) 0 mm recession, b) 3 mm recession, c) 6 mm recession and d) 9 mm recession.

Table 2
Fitting parameters of a simplified Randles circuit for deposit-covered specimen after 20 h of corrosion in a 50 °C, pH 4, CO_2 saturated, 20 g L^{-1} NaCl electrolyte.

Specimen recession	Parameter	4 h	8 h	12 h	16 h	20 h
0 mm	**R_e ($\Omega.cm^{-2}$)**	23.5 ± 2.0	24.1 ± 2.3	25.2 ± 4.3	24.8 ± 5.1	27.5 ± 6.4
	α_{dl}	0.80 ± 0.01	0.81 ± 0.02	0.81 ± 0.03	0.81 ± 0.04	0.83 ± 0.04
	Q_{dl} / 10^{-4} ($F.cm^{-2})^{\alpha}$	3.8 ± 0.5	3.8 ± 0.4	4.1 ± 0.6	4.3 ± 0.7	4.0 ± 0.6
	R_{ct} ($\Omega.cm^{-2}$)	345.1 ± 4.8	340.0 ± 80.2	368.5 ± 92.5	338.3 ± 69.1	386.4 ± 70.2
	C_{dl} ($\mu F.cm^{-2}$)	118 ± 8.0	127 ± 7.9	140 ± 15.9	148 ± 23.8	150 ± 28.4
	R_{ct}·C_{dl} (ms)	40 ± 7	38 ± 9	45 ± 9	42 ± 11	58 ± 14
	S_A (%)	100 ± 0	114 ± 6	129 ± 15	141 ± 17	147 ± 23
	Corrosion rate (mm yr^{-1})	0.9 ± 0.2	0.9 ± 0.2	0.8 ± 0.2	1.0 ± 0.4	0.8 ± 0.1
3 mm	**R_e ($\Omega.cm^{-2}$)**	27.4 ± 4.9	28.5 ± 6.4	32.1 ± 4.6	29.8 ± 5.8	31.4 ± 5.1
	α_{dl}	0.79 ± 0.03	0.80 ± 0.02	0.80 ± 0.03	0.83 ± 0.02	0.82 ± 0.03
	Q_{dl} / 10^{-4} ($F.cm^{-2})^{\alpha}$	3.2 ± 0.4	3.3 ± 0.4	3.3 ± 0.4	3.2 ± 0.3	3.2 ± 0.3
	R_{ct} ($\Omega.cm^{-2}$)	478.0 ± 159.1	428.7 ± 58.9	461.1 ± 92.1	435.7 ± 44.9	447.6 ± 37.7
	C_{dl} ($\mu F.cm^{-2}$)	94 ± 28	105 ± 23	106 ± 26	121 ± 22	124 ± 31
	R_{ct}·C_{dl} (ms)	41 ± 10	45 ± 12	49 ± 16	54 ± 14	56 ± 18
	S_A (%)	100 ± 0	136 ± 28	135 ± 21	166 ± 54	202 ± 78
	Corrosion rate (mm yr^{-1})	0.7 ± 0.3	0.7 ± 0.1	0.7 ± 0.1	0.7 ± 0.1	0.7 ± 0.1
6 mm	**R_e ($\Omega.cm^{-2}$)**	29.2 ± 2.8	31.0 ± 1.1	31.8 ± 1.5	34.5 ± 3.5	31.7 ± 0.3
	α_{dl}	0.82 ± 0.03	0.82 ± 0.01	0.83 ± 0.01	0.82 ± 0.03	0.82 ± 0.03
	Q_{dl} / 10^{-4} ($F.cm^{-2})^{\alpha}$	3.4 ± 0.4	3.7 ± 0.5	3.9 ± 0.3	4.0 ± 0.4	3.9 ± 0.4
	R_{ct} ($\Omega.cm^{-2}$)	496.9 ± 50.2	472.8 ± 85.4	584.3 ± 48.5	547.0 ± 61.8	524.0 ± 76.6
	C_{dl} ($\mu F.cm^{-2}$)	124 ± 27	140 ± 27	152 ± 26	155 ± 32	155 ± 39
	R_{ct}·C_{dl} (ms)	69 ± 23	67 ± 21	82 ± 23	85 ± 21	79 ± 16
	S_A (%)	100 ± 0	112 ± 8	121 ± 9	126 ± 12	123 ± 11
	Corrosion rate (mm yr^{-1})	0.6 ± 0.1	0.6 ± 0.1	0.6 ± 0.1	0.5 ± 0.1	0.6 ± 0.1
9 mm	**R_e ($\Omega.cm^{-2}$)**	30.8 ± 0.1	34.3 ± 0.8	38.4 ± 1.9	37.6 ± 0.5	39.6 ± 1.0
	α_{dl}	0.82 ± 0.002	0.82 ± 0.004	0.82 ± 0.002	0.83 ± 0.008	0.84 ± 0.009
	Q_{dl} / 10^{-4} ($F.cm^{-2})^{\alpha}$	3.6 ± 0.6	3.9 ± 0.7	4.0 ± 0.7	4.0 ± 0.7	4.0 ± 0.7
	R_{ct} ($\Omega.cm^{-2}$)	859.2 ± 4.9	636.9 ± 93.0	627.4 ± 55.2	575.4 ± 79.4	585.0 ± 89.3
	C_{dl} ($\mu F.cm^{-2}$)	134 ± 26	151 ± 29	159 ± 31	172 ± 35	178 ± 37
	R_{ct}·C_{dl} (ms)	92 ± 16	93 ± 6	99 ± 14	81 ± 1	84 ± 2
	S_A (%)	100 ± 0	112 ± 4	119 ± 5	128 ± 6	132 ± 5
	Corrosion rate (mm yr^{-1})	0.5 ± 0.2	0.5 ± 0.1	0.5 ± 0.04	0.5 ± 0.1	0.5 ± 0.1

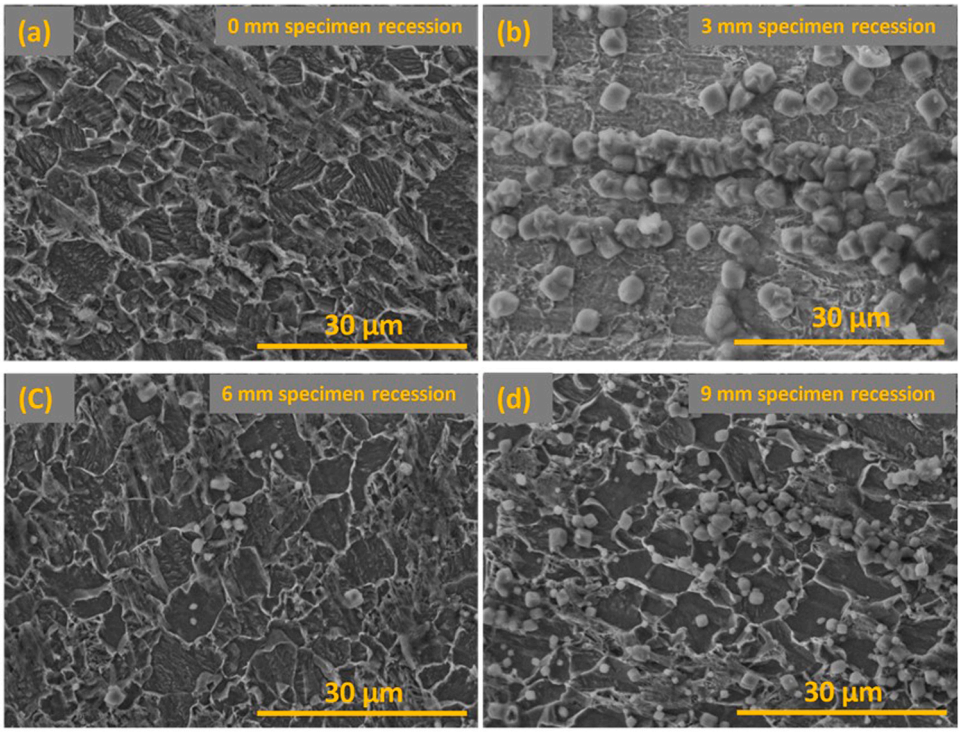

Fig. 11. SEM images taken on Hitachi TM3030Plus Autostage SEM at 2500X magnification of under deposit X65 carbon steel specimen (covered with SiO_2 deposit) after 20 h of corrosion in a 50 °C, pH 4, CO_2 saturated, 20 g L^{-1} NaCl electrolyte. a) 0 mm recession, b) 3 mm recession, c) 6 mm recession and d) 9 mm recession.

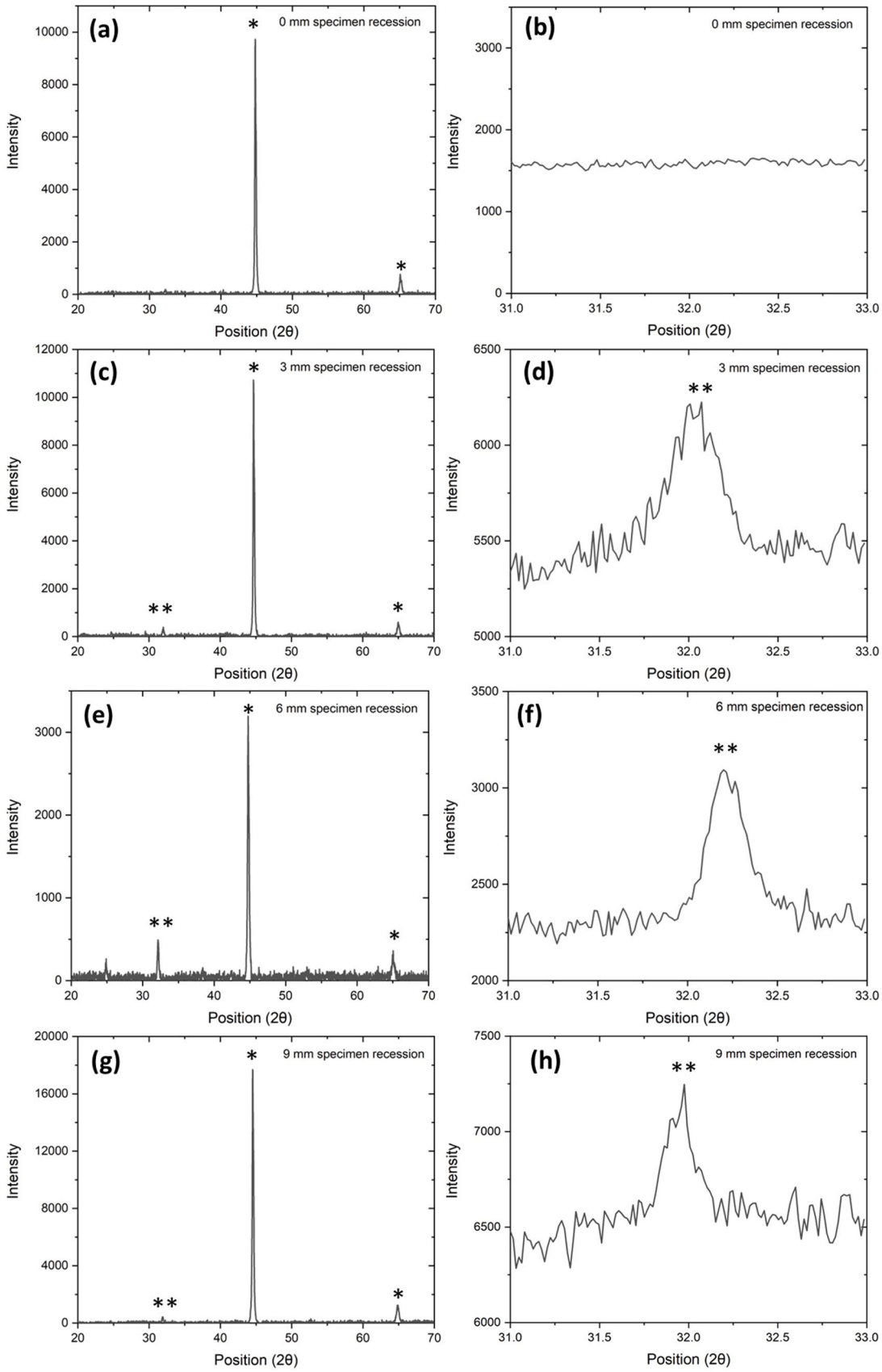

Fig. 12. XRD pattern for specimens corroding under a SiO_2 deposit taken after 20 h of corrosion in a 50 °C, pH 4, CO_2 saturated, 20 g L^{-1} NaCl electrolyte. (a), (c), (e), (g) taken in a scan range of 20–70°. (b), (d), (f), (h) taken in the scan range of 31–33° to enhance the $FeCO_3$ peak. Where, * represents Fe and * * $FeCO_3$.

imaging above. The visual representations provided here support the EIS results presented earlier. The higher value of R_{ct} observed, could in some part, be due to the formation of $FeCO_3$. Additionally, the increase in S_a was smaller over the duration of the test when a SiO_2 deposit was present, this may be due to the formation of $FeCO_3$ which blocks the active anodic and cathodic reactive sites [25].

3.5. Galvanic corrosion

Galvanic corrosion between uncovered and covered specimens in the absence of an inhibitor has been assessed in literature with the under deposit specimen typically acting as a net cathode when coupled to a specimen entirely exposed to electrolyte [6,10]. In this experiment, the current and potential between the two specimens were recorded every second for 20 h to identify changes in corrosion behaviour. Electrochemical results (Fig. 3) demonstrated minimal variation in corrosion rate between different specimen recessions. However, post experimental surface analysis revealed changes in surface properties between specimens with and without recession. Therefore, the two extremes in recession depth (0 mm and 9 mm) were assessed for their galvanic corrosion behaviour. The galvanic corrosion current density and galvanic corrosion potential between specimens under an SiO_2 deposit layer (at 0 mm and 9 mm specimen recession) coupled with a specimen entirely exposed to electrolyte (area ratio 1:18) are shown in Fig. 13. The averages are shown from a minimum of 3 repeat measurements.

The galvanic current density (calculated using the surface area of the under deposit specimen, 0.28 cm^{-2}) and galvanic corrosion potential have been provided in Fig. 13. Little difference in performance was identified between recession depths with the current remaining in the negative region for the duration of the test. The under-deposit specimen acted as the net cathode in all cases. The galvanic potential increases slightly with time as conductive FeC_3 is revealed which increases corrosion rates. This result corroborated with the results presented by Barker *et al.* [10].

The visual effects of galvanic corrosion were assessed using SEM (Fig. 14). The under deposit specimen at 0 mm depth showed little difference to the uncoupled specimen (Fig. 11) indicating minimal change in corrosion rate. The specimen at 9 mm recession, showed $FeCO_3$ crystals on the surface, whilst the exposed specimen in both cases showed a dense network of Fe_3C, as expected.

3.6. pH measurements within recessed regions

The SEM images provided revealed the unexpected formation of $FeCO_3$. At pH 4, the formation of $FeCO_3$ is unlikely due to the high local concentration of Fe^{2+} required to achieve sufficient local supersaturation for precipitation to occur [25]. This was shown by Pessu *et al.* [43], who were unable to form $FeCO_3$ within 36 h on carbon steel corroding in a 50 °C, pH 3.8, CO_2 saturated, 35 g L^{-1} NaCl electrolyte. When the bulk electrolyte pH was increased to 6.6, discrete $FeCO_3$ crystals formed on the steel surface, attributed to the significant reduction in the concentration of Fe^{2+} required to reach supersaturation [44]. This gives reasonable cause to believe near surface pH increased significantly in under deposit environments.

To verify the increase in pH when a deposit is present, in-situ real time pH measurements were recorded and shown in Fig. 15. The bulk electrolyte pH, without any corrosion processes occurring remained constant at 4.1. In the absence of a deposit, the pH at both 0 mm and 9 mm recession was stable at 4.1 for the duration of the 20 h test. At this pH, $FeCO_3$ formation is unlikely, as confirmed by SEM imaging (Fig. 10) where crystal formation was not identified.

The pH in the presence of the deposit at 0 mm specimen recession gradually increased from pH 4.3 to pH 5.3, with an average pH of 5.25 ± 0.26. At 9 mm specimen recession the pH was stable at 5.9 ± 0.1, an increase of 2.8 from the bulk electrolyte. These results are in agreement with Han *et al.* [21] where the introduction of a 5 mm sand layer on a carbon steel specimen in a CO_2 saturated, 10 g L^{-1} NaCl electrolyte at 20 °C resulted in a surface pH increase of 2.3 from the bulk. Dugstad *et al.* [44] demonstrated that the concentration of Fe^{2+} required for $FeCO_3$ precipitation decreased by ~57% between pH 4 and pH 5.25, and a further 40% when pH increased to 5.9 [25,44]. Therefore, the pH within a recess with a deposit falls within the range where $FeCO_3$ precipitation is possible, particularly at greater recession depths.

However, despite $FeCO_3$ precipitation occurring, a dense protective layer did not form, and no reduction in corrosion rate as a result of $FeCO_3$ was observed. It is important to note that the pH increase at 0 mm specimen recession could, in some cases, lead to heterogenous $FeCO_3$ precipitation.

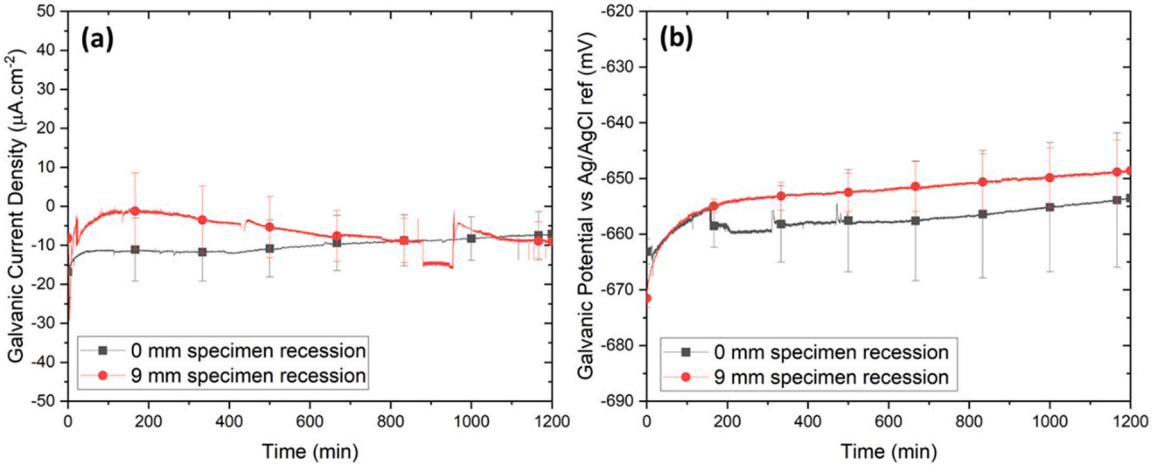

Fig. 13. (a) Galvanic corrosion current density and (b) mixed galvanic potential between a covered X65 carbon steel specimen with a surface area of 0.28 cm^2 at 0 mm specimen recession (black) and 9 mm specimen recession (red) coupled to an exposed specimen with a surface area of 4.9 cm^{-2}. All specimens are corroding in a 50 °C, pH 4, CO_2 saturated, 20 g L^{-1} NaCl electrolyte.

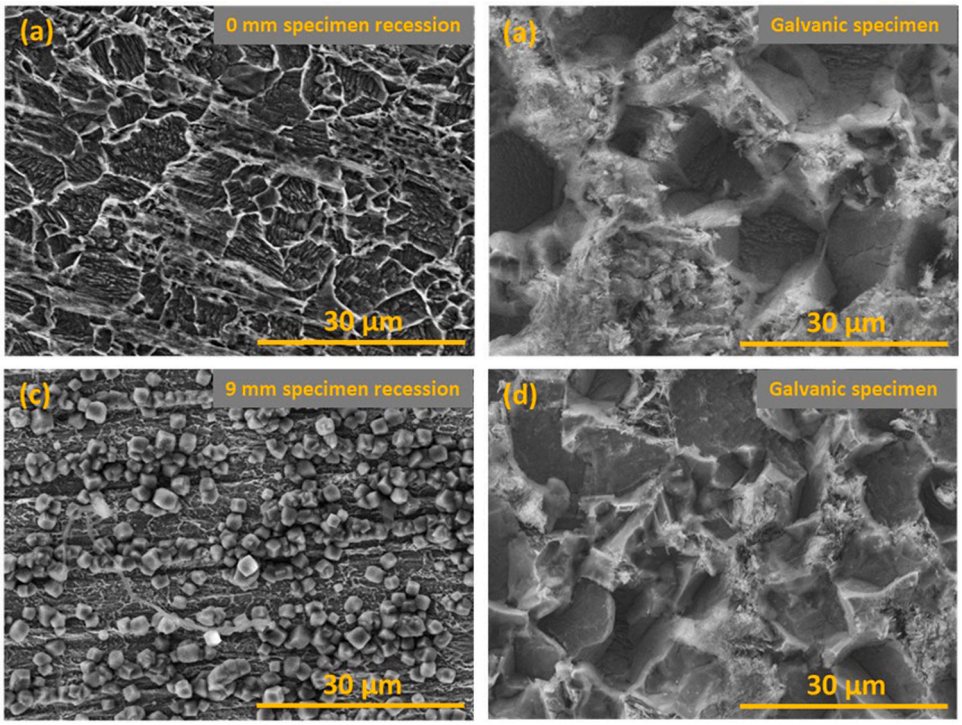

Fig. 14. SEM images of coupled X65 specimen taken after 20 h of corrosion in a 50 °C, pH 4, CO_2 saturated, 20 g L^{-1} NaCl electrolyte. (a) WE 1 at 0 mm specimen recession under deposit, (b) WE 2 in bulk solution coupled to a, (c) WE1 at 9 mm specimen recession under deposit and (d) WE 2 in bulk solution coupled to b. Images were acquired on a Hitachi benchtop SEM in BSE mode and 2500X magnification.

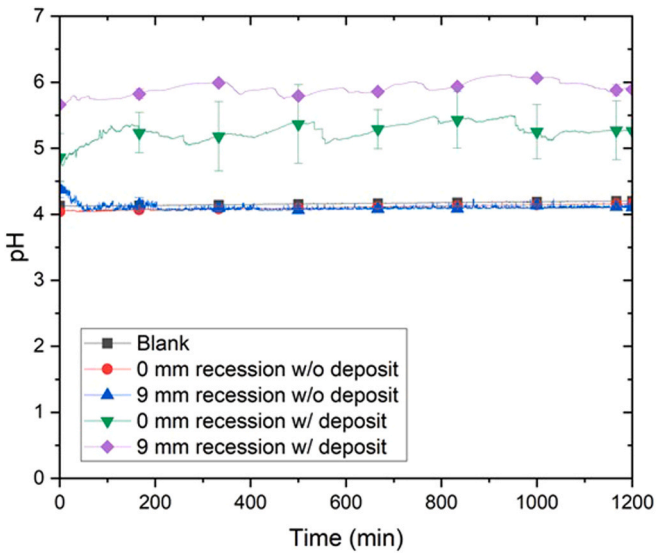

Fig. 15. pH measurements recorded at 2 s intervals with a Mettler Toledo Inlab NMR pH probe, in a 50 °C, pH 4, CO_2 saturated, 20 g L^{-1} NaCl electrolyte. In bulk solution without a specimen (black), in the absence of deposit at 0 mm recession (red) and 9 mm recession (blue), in the presence of deposit at 0 mm specimen recession (green), and 9 mm specimen recession (purple).

4. Conclusion

The effect of thick SiO_2 deposit layers on the corrosion behaviour of deep pit-like features was examined using X65 carbon steel at various recession depths in a bespoke test cell. Experiments were performed in a CO_2-saturated, pH 4 solution containing 20 g L^{-1} of NaCl and corrosion behaviour was monitored using a range of electrochemical techniques. The following conclusions were drawn:

- A bespoke test cell was developed which enabled in-situ electrochemical measurements of under deposit localised corrosion and galvanic corrosion. Additionally, the cell was used to evaluate pH changes within a recessed region with and without SiO_2 deposit.
- The presence of a thick SiO_2 deposit layer reduced corrosion rates from ~3.5 mm yr^{-1} to 1 mm yr^{-1} at all recession depths. This was related to the deposit potentially acting as a diffusion barrier restricting the movement of corrosive ions to and from the metal surface.
- In the absence of a deposit, corrosion rates were similar at all recession depths, increasing over the duration of the experiment due to the revealing of an Fe_3C network and its contribution in the galvanic coupling.
- When a deposit was present EIS was used to evaluate the corrosion rate decreases over time, in particular when the recession depth exceeded 3 mm. This was attributed to the formation of $FeCO_3$, verified using SEM.
- Galvanic corrosion measurements highlighted the under deposit specimen was the net cathode in the galvanic couple.
- The pH within a recess under a deposit was measured using a milli pH probe, indicating the local electrolyte chemistry under the deposit was vastly different to the bulk solution, with an increase in pH from 4.1 to 5.9 providing conditions favouring the precipitation of $FeCO_3$. This increase in pH was most significant at a recession depth of 9 mm.

CRediT authorship contribution statement

Bernard Normand: Formal analysis, Writing – review & editing. **Sabrina Marcelin:** Formal analysis, Writing – review & editing. **Michael Huggan:** Methodology. **Joshua Owen:** Conceptualization, Formal analysis, Methodology, Writing – review & editing, Supervision.

Raeesa Bhamji: Conceptualization, Data curation, Formal analysis, Investigation, Methodology, Writing – original draft, Writing – review & editing. **Richard Barker:** Conceptualization, Formal analysis, Funding acquisition, Methodology, Supervision, Writing – review & editing.

Declaration of Competing Interest

The authors declare that they have no known competing financial interests or personal relationships that could have appeared to influence the work reported in this paper.

Data availability

Data forms part of ongoing study.

Acknowledgements

The authors would like to acknowledge funding from Engineering and Physical Sciences Research Council and Shell UK Ltd. A special mention to Paulina Czerwinska, Shell UK, for her contribution in reviewing the manuscript.

Appendix A. Supporting information

Supplementary data associated with this article can be found in the online version at doi:10.1016/j.corsci.2023.111744.

References

[1] J.R. Vera D. Daniels M.H. Achour Under deposit corrosion (UDC) in the oil and gas industry: a review of mechanisms, testing and mitigation. In: CORROSION 2012, Salt Lake City, Utah. NACE International, 2012.
[2] Z.B. Wang, L. Pang, Y.G. Zheng, A review on under-deposit corrosion of pipelines in oil and gas fields: testing methods, corrosion mechanisms and mitigation strategies, Corros. Commun. 7 (2022) 70–81.
[3] A. Lazareva, J. Owen, S. Vargas, R. Barker, A. Neville, Investigation of the evolution of an iron carbonate layer and its effect on localized corrosion of X65 carbon steel in CO_2 corrosion environments, Corros. Sci. 192 (2021), 109849.
[4] W. Durnie, M. Gough, H. De Reus, Development of corrosion inhibitors to address under deposit corrosion in oil and gas production systems, Corros. 2005 NACE Int. (2005).
[5] J. Huang, B. Brown, X. Jiang, B. Kinsella, S. Nesic, Internal CO_2 corrosion of mild steel pipelines under inert solid deposits, Corrosion 2010 (2010) NACE-10379.
[6] R. Nyborg M. Foss. Experience with an under deposit corrosion test method with galvanic current measurements. In: CORROSION 2011, Houston, Texas. NACE-11259: NACE International, 2011.
[7] V. Pandarinathan, K. Lepková, Van Bronswijk, W. Chukanovite, $(Fe_2(OH)_2CO_3)$ identified as a corrosion product at sand-deposited carbon steel in CO_2-saturated brine, Corros. Sci. 85 (2014) 26–32.
[8] Turnbull, A., Coleman, D., Griffiths, A.J., Francis, P.E. and Orkney, L. Effectiveness of corrosion inhibitors in retarding the rate of propagation of localized corrosion. In: CORROSION 2003, 2003/03/01, San Diago, California NACE International, 2003, pp.250–257.
[9] A. Pedersen K. Bilkova E. Gulbrandsen J. Kvarekvål CO_2 corrosion inhibitor performance in the presence of solids: test method development. In: CORROSION 2008, New Orleans, Louisiana. NACE International, 2008.
[10] Barker, R., Pickles, B. and Neville, A. General corrosion of X65 steel under silica sand deposits in CO_2-saturated environments in the presence of corrosion inhibitor components. In: CORROSION 2014, Detroit. NACE International, 2014.
[11] Huang, J., Brown, B., Nesic, S., Papavinasam, S. and Gould, D. Localized corrosion of mild steel under silica deposits in inhibited aqueous CO_2 solutions. In: CORROSION 2013, Orlando, Florida. NACE International, 2013, p.2144.
[12] G. Hinds, P. Cooling, S. Zhou, A. Turnbull, Underdeposit test method for assessing performance of corrosion inhibitors. Eurocorr, 2008, pp. 1–11.
[13] Turnbull, A., Hinds, G., Cooling, P. and Zhou, S. A multi-electrode approach to evaluating inhibition of underdeposit corrosion in CO_2 environments. In: CORROSION 2009, Atlanta, Georgia. NACE International 2009.
[14] De Reus, H., Hendriksen, L.J.A., Wilms, M., Al-Habsi, Y.N., Durnie, W. and Gough, M. Test Methodologies and field verification of corrosion inhibitors to address under deposit corrosion in oil and gas production systems. In: CORROSION 2005, NACE-05288, 2005.
[15] G.Z. Meng, C. Zhang, Y.F. Cheng, Effects of corrosion product deposit on the subsequent cathodic and anodic reactions of X-70 steel in near-neutral pH solution, Corros. Sci. 50 (11) (2008) 3116–3122.
[16] J. Galvele, Transport processes in passivity breakdown—II. Full hydrolysis of the metal ions, Corros. Sci. 21 (8) (1981) 551–579.
[17] R.C. Newman, The dissolution and passivation kinetics of stainless alloys containing molybdenum—II. Dissolution kinetics in artificial pits, Corros. Sci. 25 (5) (1985) 341–350.
[18] J. Amri, E. Gulbrandsen, R.P. Nogueira, Pit growth and stifling on carbon steel in CO_2-containing media in the presence of HAc, Electrochim. Acta 54 (28) (2009) 7338–7344.
[19] G. Hinds, A. Turnbull, Novel multi-electrode test method for evaluating inhibition of underdeposit corrosion—part 1: sweet conditions, Corrosion 66 (4) (2010), 046001-046001-046010.
[20] Zhang,Y., Moloney, J. and Mancuso, S. Understanding Factors Affecting CorrosionInhibitor Performance in Under-Deposit Testing with Sand. In: CORROSION 2013, Orlando, Florida. NACE International,2013.
[21] D. Pope, T. Zintel, Methods for investigating underdeposit microbiologically influenced corrosion: a review, Mater. Perform. 28 (11) (1989) 46–51.
[22] J. Han, B.N. Brown, D. Young, S. Nešić, Mesh-capped probe design for direct pH measurements at an actively corroding metal surface, J. Appl. Electrochem. 40 (3) (2010) 683–690.
[23] J. Han, D. Young, H. Colijn, A. Tripathi, S. Nešić, Chemistry and structure of the passive film on mild steel in CO_2 corrosion environments, Ind. Eng. Chem. Res. 48 (13) (2009) 6296–6302.
[24] A. Shamsa, R. Barker, Y. Hua, E. Barmatov, T.L. Hughes, A. Neville, Performance evaluation of an imidazoline corrosion inhibitor in a CO_2-saturated environment with emphasis on localised corrosion, Corros. Sci. 176 (2020), 108916.
[25] R. Barker, A. Neville, X. Hu, S. Cushnaghan, Evaluating inhibitor performance in CO_2-saturated erosion-corrosion environments, Corrosion 71 (1) (2014) 14–29.
[26] Owen, J., Joshi, G.R., Barker, R., Ropital, F. and Kittel, J. Galvanic Interactions Between Surface Layers and Bare Carbon Steel in Aqueous CO_2 Environments. In: AMPP Annual Conference+ Expo, San Antonio, Texas OnePetro, 2022.
[27] R. Barker, D. Burkle, T. Charpentier, H. Thompson, A. Neville, A review of iron carbonate $(FeCO_3)$ formation in the oil and gas industry, Corros. Sci. 142 (2018) 312–341.
[28] I. Azoulay, C. Rémazeilles, P. Refait, Determination of standard Gibbs free energy of formation of chukanovite and Pourbaix diagrams of iron in carbonated media, Corros. Sci. 58 (2012) 229–236.
[29] Watson, W. and Orazem, M.E. EIS: measurement model program, 2020.
[30] Farelas, F., Brown, B. and Nesic, S. Iron carbide and its influence on the formation of protective iron carbonate in CO2 corrosion of mild steel. In: CORROSION, Orlando, Florida. OnePetro, 2013.
[31] J. Owen, F. Ropital, G.R. Joshi, J. Kittel, R. Barker, Galvanic effects induced by siderite and cementite surface layers on carbon steel in aqueous CO_2 environments, Corros. Sci. 209 (2022), 110762.
[32] F. Farelas, M. Galicia, B. Brown, S. Nesic, H. Castaneda, Evolution of dissolution processes at the interface of carbon steel corroding in a CO_2 environment studied by EIS, Corros. Sci. 52 (2) (2010) 509–517.
[33] J.L. Crolet, N. Thevenot, S. Nesic, Role of conductive corrosion products in the protectiveness of corrosion layers, Corrosion 54 (3) (1998) 194–203.
[34] M.E. Orazem, Underground pipeline corrosion: detection, analysis and prevention. Sawston [Cambridgeshire, Elsevier Woodhead Publishing,, 2014.
[35] B.A. Boukamp, A linear Kronig-Kramers transform test for immittance data validation, J. Electrochem. Soc. 142 (6) (1995) 1885.
[36] Orazem, M.E. and Tribollet, B. Electrochemical impedance spectroscopy. Hoboken, N.J: Wiley, 2008.
[37] R.L. Hurt, J.R. Macdonald, Distributed circuit elements in impedance spectroscopy: a unified treatment of conductive and dielectric systems, Solid State Ion. 20 (2) (1986) 111–124.
[38] R. De Motte, R. Mingant, J. Kittel, F. Ropital, P. Combrade, S. Necib, V. Deydier, D. Crusset, Near surface pH measurements in aqueous CO_2 corrosion, Electrochim. Acta 290 (2018) 605–615.
[39] R. De Motte, E. Basilico, R. Mingant, J. Kittel, F. Ropital, P. Combrade, S. Necib, V. Deydier, D. Crusset, S. Marcelin, A study by electrochemical impedance spectroscopy and surface analysis of corrosion product layers formed during CO_2 corrosion of low alloy steel, Corros. Sci. 172 (2020), 108666.
[40] P. Bommersbach, C. Alemany-Dumont, J.P. Millet, B. Normand, Formation and behaviour study of an environment-friendly corrosion inhibitor by electrochemical methods, Electrochim. Acta 51 (6) (2005) 1076–1084.
[41] P. Han, C. Chen, W. Li, H. Yu, Y. Xu, L. Ma, Y. Zheng, Synergistic effect of mixing cationic and nonionic surfactants on corrosion inhibition of mild steel in HCl: experimental and theoretical investigations, J. Colloid Interface Sci. 516 (2018) 398–406.
[42] G. Brug, A.L. van den Eeden, M. Sluyters-Rehbach, J.H. Sluyters, The analysis of electrode impedances complicated by the presence of a constant phase element, J. Electroanal. Chem. Interfacial Electrochem. 176 (1–2) (1984) 275–295.
[43] B. Kinsella, Y.J. Tan, S. Bailey, Electrochemical impedance spectroscopy and surface characterization techniques to study carbon dioxide corrosion product scales, Corrosion 54 (10) (1998) 835–842.
[44] B. Hirschorn, M.E. Orazem, B. Tribollet, V. Vivier, I. Frateur, M. Musiani, Determination of effective capacitance and film thickness from constant-phase-element parameters, Electrochim. Acta 55 (21) (2010) 6218–6227.

Further reading

[1] O. Devos, C. Gabrielli, B. Tribollet, Simultaneous EIS and in situ microscope observation on a partially blocked electrode application to scale electrodeposition, Electrochim. Acta 51 (8) (2006) 1413–1422.

[2] S. Hoseinieh, A. Homborg, T. Shahrabi, J. Mol, B. Ramezanzadeh, A novel approach for the evaluation of under deposit corrosion in marine environments using combined analysis by electrochemical impedance spectroscopy and electrochemical noise, Electrochim. Acta 217 (2016) 226–241.

[3] F. Pessu, R. Barker, A. Neville, The Influence of pH on Localized Corrosion Behavior of X65 Carbon Steel in CO_2-saturated brines, Corrosion 71 (12) (2015) 1452–1466.

[4] Dugstad, A. Fundamental aspects of CO_2 metal loss corrosion-part 1: mechanism. In: NACE 2006, San Diego, California NACE INTERNATIONAL, 2006.